ARMY RESEARCH LABORATORY

# Prediction of Projectile Performance, Stability, and Free-Flight Motion Using Computational Fluid Dynamics

## by Paul Weinacht

**ARL-TR-3015**                                                            **July 2003**

20030929 070

## NOTICES

### Disclaimers

# Army Research Laboratory
Aberdeen Proving Ground, MD 21005-5066

# Prediction of Projectile Performance, Stability, and Free-Flight Motion Using Computational Fluid Dynamics

**Paul Weinacht**
**Weapons and Materials Research Directorate, ARL**

| REPORT DOCUMENTATION PAGE | | Form Approved OMB No. 0704-0188 |
|---|---|---|

| 1. REPORT DATE (DD-MM-YYYY) | 2. REPORT TYPE | 3. DATES COVERED (From - To) |
|---|---|---|
| July 2003 | Final | 1997–2002 |

| 4. TITLE AND SUBTITLE | 5a. CONTRACT NUMBER |
|---|---|
| Prediction of Projectile Performance, Stability, and Free-Flight Motion Using Computational Fluid Dynamics | |
| | 5b. GRANT NUMBER |
| | 5c. PROGRAM ELEMENT NUMBER |

| 6. AUTHOR(S) | 5d. PROJECT NUMBER |
|---|---|
| Paul Weinacht | 1L1612618AH80 |
| | 5e. TASK NUMBER |
| | 5f. WORK UNIT NUMBER |

| 7. PERFORMING ORGANIZATION NAME(S) AND ADDRESS(ES) | 8. PERFORMING ORGANIZATION REPORT NUMBER |
|---|---|
| U.S. Army Research Laboratory ATTN: AMSRL-WM-BC Aberdeen Proving Ground, MD 21005-5066 | ARL-TR-3015 |

| 9. SPONSORING/MONITORING AGENCY NAME(S) AND ADDRESS(ES) | 10. SPONSOR/MONITOR'S ACRONYM(S) |
|---|---|
| | 11. SPONSOR/MONITOR'S REPORT NUMBER(S) |

**12. DISTRIBUTION/AVAILABILITY STATEMENT**

Approved for public release; distribution is unlimited.

**13. SUPPLEMENTARY NOTES**

**14. ABSTRACT**

With the recent development of capabilities for predicting the damping derivatives, it is now possible to predict the stability characteristics and free-flight motion for projectiles using data that are derived solely from computational fluid dynamics (CFD). As a demonstration of the capability, this report presents results for a family of axisymmetric projectiles in supersonic flight. The particular configuration selected for this computational study has been extensively tested in aeroballistic ranges, and high-quality experimental data have been obtained. Thin-layer Navier-Stokes techniques have been applied to compute the attached viscous flow over the forebody of the projectile and the separated flow in the projectile base region. Using the predicted aerodynamics coefficients, parameters that characterize the in-flight motion are subsequently evaluated, including the gyroscopic and dynamic stability factors, and the projectile's fast and slow mode frequencies and damping coefficients. These parameters are then used to predict the free-flight motion of the projectile. In each case, the computational approach is validated by comparison with experimental data, and very good agreement between computation and experiment is found. It is believed that this demonstration represents the first known instance of a viscous CFD approach being applied to predict all the necessary data for performance of linear aerodynamics stability and trajectory analyses.

**15. SUBJECT TERMS**

computational fluid dynamics, projectile aerodynamics, flight mechanics

| 16. SECURITY CLASSIFICATION OF: | | | 17. LIMITATION OF ABSTRACT | 18. NUMBER OF PAGES | 19a. NAME OF RESPONSIBLE PERSON Paul Weinacht |
|---|---|---|---|---|---|
| a. REPORT | b. ABSTRACT | c. THIS PAGE | UL | 32 | 19b. TELEPHONE NUMBER (Include area code) (410) 278-4280 |
| UNCLASSIFIED | UNCLASSIFIED | UNCLASSIFIED | | | |

# Contents

# List of Figures

# 1. Introduction

Prediction of the in-flight motion of projectiles requires the determination of the aerodynamic forces and moments that act on the body during the course of its trajectory. These aerodynamic forces and moments may be determined from free-flight aerodynamics ranges (*1*), wind tunnel experiments (*2*), or theoretical approaches, such as computational fluid dynamics (CFD). In the supersonic flight regime, static aerodynamic coefficients such as drag and pitching moment have been routinely computed using CFD for a number of years (*3, 4*). Much less routine are predictions of dynamic aerodynamic coefficients, such as the pitch damping and Magnus coefficients. A computational capability for predicting the Magnus forces and moments for smooth medium- and large-caliber flight bodies has existed since the early 1980s (*3, 4*). With the recent development of capabilities for predicting the damping derivatives (*5*), it is now possible to predict the stability characteristics and free-flight motion for projectiles using data that are derived solely from CFD.

While previous research work has focused on predictions of the individual aerodynamic coefficients, this report focuses on the predictions of aerodynamic performance, in particular, aerodynamic stability. This report attempts to demonstrate, through a particular case study, the suitability and accuracy of Navier-Stokes computational techniques for the prediction of projectile performance and stability. Until recently, this was not possible since methods had not been implemented to predict all the necessary coefficients.

As a demonstration of the capability, this report will present results for a family of axisymmetric projectiles in supersonic flight. The particular configuration selected for this computational study has been extensively tested in aeroballistic ranges, and high-quality experimental data have been obtained (*1*). The configuration consists of 5-, 7-, and 9-caliber length versions. By varying the mass distribution, three different centers of gravity (CG) were tested for each body length. A schematic of the configuration is shown in Figure 1.

The computational results were obtained by applying a parabolized Navier-Stokes (PNS) approach to compute the attached viscous flow over the forebody of the projectile. Aerodynamic forces and moments were then extracted from the computed flow fields by integration of the predicted pressure and shear stresses acting on the projectile surface. To compute the recirculating flow at the base of the projectile and subsequently the base drag, a time-marching Navier-Stokes approach was applied.

Using the predicted aerodynamics coefficients, parameters that characterize the in-flight motion are subsequently evaluated, including the gyroscopic and dynamic stability factors and the projectile's fast and slow mode frequencies and damping coefficients. These parameters are then

Figure 1. Schematic of Army-Navy Spinner rocket (ANSR) configuration.
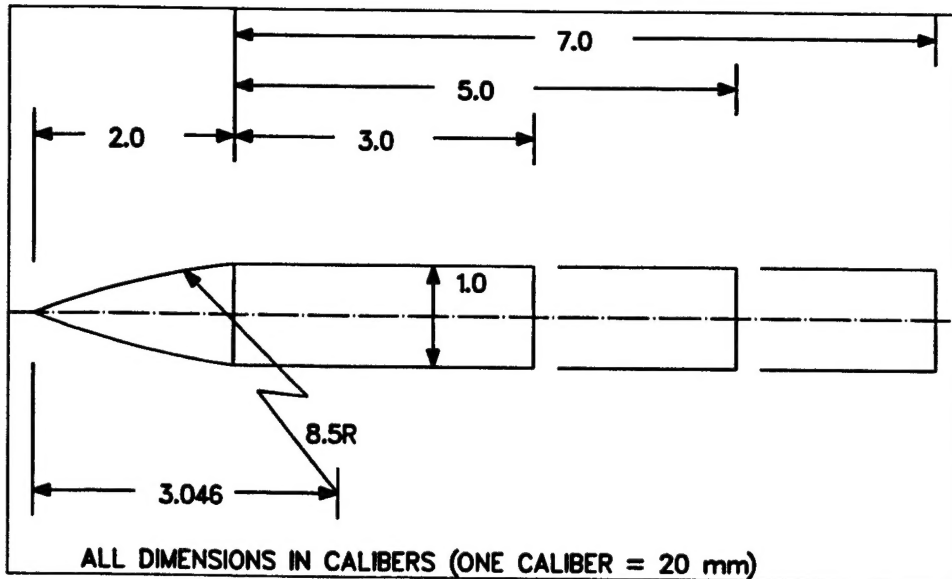
used to predict the free-flight motion of the projectile. In each case, the computational approach is validated by comparison with experimental data.

## 2. Computational Approach

The supersonic viscous flow field about the projectile configuration was obtained by applying a parabolized Navier-Stokes technique to determine the attached flow field over the projectile forebody and a time-marching Navier-Stokes technique to determine the recirculating flow in the base region. Both of these numerical techniques are briefly described in the following subsections.

### 2.1 The PNS Approach

Computation of the attached viscous flow field about the projectile forebody was accomplished by solving the thin-layer Navier-Stokes equations using the PNS technique of Schiff and Steger (6). Using the PNS technique, computational results are obtained by marching through the grid from the projectile nose to the base. This technique is applicable in the supersonic flow regime and requires that the flow field contain no regions of flow separation in the axial direction. Because the computational approach requires only a single sweep through the computational grid, it is very efficient, compared with time-marching approaches that require many sweeps through the grid.

As is standard practice, prediction of the static aerodynamic coefficients, such as pitching moment and normal force coefficients, are performed by computing the flow field about the projectile at a constant angle of attack. The Magnus coefficients are obtained from a

2

computation of the flow field at a constant angle of attack and spin rate. Since the static aerodynamics for spinning axisymmetric bodies are generally invariant with spin rate, it is possible to obtain the static aerodynamic coefficients and the Magnus coefficients from a single computation. The pitch-damping coefficients are determined from the side force and moment acting on the projectile undergoing steady coning motion. Steady coning motion is defined as the motion performed by a missile flying at a constant angle with respect to the freestream velocity vector and undergoing a rotation at a constant angular velocity about a line parallel to the freestream velocity vector and coincident with the projectile's CG. Coning motion is, in fact, a specific combination of two orthogonal planar pitching motions plus a spinning motion. From linear flight mechanics theory, it can be shown that the pitch-damping coefficients are related to the side force and moment due to steady coning motion (5).

The flow field predictions of the projectile in steady coning motion have been performed in a novel rotating coordinate frame that rotates at the roll rate or coning rate of the projectile. The fluid flow relative to the rotating coordinate frame does not vary with time, allowing the steady (non-time varying) Navier-Stokes equations to be applied. To implement the rotating coordinate frame, the governing equations have been modified to include the effect of centrifugal and Coriolis forces. The steady, thin-layer Navier-Stokes equations are shown in equation 1:

$$\frac{\partial \hat{E}}{\partial \xi} + \frac{\partial \hat{F}}{\partial \eta} + \frac{\partial \hat{G}}{\partial \zeta} + \hat{H} = \frac{1}{Re} \frac{\partial \hat{S}}{\partial \zeta}. \tag{1}$$

Here, $\hat{E}$, $\hat{F}$, and $\hat{G}$ are the inviscid flux vectors, $\hat{S}$ is the viscous flux vector, and $\hat{H}$ is the source term containing the Coriolis and centrifugal force terms, which result from the rotating coordinate frame. Each of these matrices is a function of the dependent variables represented by the vector q($\rho$, $\rho$u, $\rho$v, $\rho$w, e), where $\rho$ and e are the density and the total energy per unit volume, and u, v, and w, are the velocity components in x, y, and z directions. Further details of the flux terms and the source term containing the Coriolis and centrifugal forces are given by Schiff and Steger (6) and Weinacht et al. (5), respectively.

The thin-layer equations are solved using the PNS technique of Schiff and Steger (6). Following the approach of Schiff and Steger, the governing equations, which have been modified here to include the Coriolis and centrifugal force terms, are solved using a conservative, approximately factored, implicit finite-difference numerical algorithm as formulated by Beam and Warming (7). A fully turbulent boundary layer has been modeled using the Baldwin-Lomax turbulence model (8).

The computations presented here were performed using a shock-fitting procedure reported by Rai and Chaussee (9). This procedure solves the five Rankine-Hugoniot jump conditions, two geometric shock-propagation conditions, and one compatibility equation to determine the values of the five dependent variables immediately behind the shock, as well as the position of the

3

shock. The shock-fitting procedure was appropriately modified when coning motion was employed (5).

The computational results presented here were obtained using a grid that consisted of 60 points between the body and the shock. In the circumferential direction, gridding was performed over the entire body 360° using 36 points spaced at 10° increments. Approximately 75 axial marching steps were used for each caliber of body length. Because several of the aerodynamic coefficients are strongly influenced by viscous effects, the boundary layer was adapted by monitoring the nondimensional boundary layer coordinate, $y^+$, along the leeside of the body and adjusting the normal grid spacing so that the $y^+$ was ~3. This approach has been successfully applied in previous studies (3).

The computations have been performed on a variety of computer platforms. Typical solutions for a single set of conditions (Mach number, coning rate, angle of attack, etc.) required 5–10 min total CPU time on a Cray SV1 computer.

The selection of grid parameters for the current study is consistent with those used in the previous studies that focused on the individual aerodynamics coefficients (3–5). The grid requirements shown in these previous studies indicate that accurate results for the complete set of aerodynamics coefficient can be obtained with a single grid. As part of the current effort, a grid refinement study for the length-to-diameter-ratio ([L/D] = 9) body, middle CG position was also performed. A more refined grid with 90 points between the body and the shock, 72 circumferential points and 150 axial marching steps for each caliber of body length was utilized. A comparison of the results obtained with the baseline and refined grids indicated a maximum difference of <1.5% between the two complete sets of aerodynamic coefficients.

## 2.2 The Time-Marching Approach

For the recirculating flow in the base region of the flow field, the PNS technique can no longer be used, and a more generally applicable approach such as the time-marching technique must be applied. The time-marching technique is based on the unsteady or time-dependent Navier-Stokes equations. For steady flow applications, such as those discussed here, the solution is obtained by marching an initial "guessed" solution to a final converged solution in a time-iterative manner. This requires the entire flow field to be updated at each time step and numerous time steps are required as the solution evolves to the converged steady-state result. Because of this, the time-marching approach is much more computationally intensive in terms of its run-times and computer memory requirements than the PNS technique.

For the predictions presented here, the time-dependent approach was applied to compute the axisymmetric (zero angle of attack) base flow as a means of evaluating the zero-yaw drag. The small, but measurable, effect of yaw on drag was not considered in this study. The effect of the base flow on the other coefficients was also assumed to be small.

4

The particular time-marching technique applied here is the implicit, partially flux-split, upwind numerical scheme developed by Steger and his colleagues (*10, 11*). The technique is based on the flux-splitting approach of Steger and Warming (*12*) and is often referred to as the F3D technique. The upwind scheme provides natural numerical dissipation, better stability properties and better computational efficiency compared with implicit central differencing schemes (*10–12*).

The technique is based on the time-dependent thin-layer Navier-Stokes equations shown in equation 2:

$$\frac{\partial \hat{q}}{\partial t} + \frac{\partial \hat{E}}{\partial \xi} + \frac{\partial \hat{F}}{\partial \eta} + \frac{\partial \hat{G}}{\partial \zeta} + \hat{H} = \frac{1}{Re}\frac{\partial \hat{S}}{\partial \zeta}; \tag{2}$$

The flux-splitting algorithm of the F3D approach reduces the computational requirements by eliminating one of the three implicit inversions associated with the central difference Beam-Warming algorithm (*7*). The two-factor implicit algorithm involves two sweeps through the grid at each time step. The first sweep involves inverting the block tridiagonal system of equations in the $\zeta$-direction along grid lines of constant $\xi$ and $\eta$ to determine the intermediate solution variable. During the second sweep, a second block tridiagonal system of equations is inverted in the $\eta$-direction along grid lines of constant $\xi$ and $\zeta$ to determine the dependent variable.

The particular version of the code applied here has a multizone capability that allows the computational grid to be decomposed into smaller blocks. This allows greater flexibility in gridding of flight bodies, particularly when it is desirable to preserve sharp corners. The multizone capability also allows the computer memory requirement for the computation to be reduced since only one zone needs to be in memory at a time and the other zones can be stored on disk. This capability was implemented by Sahu and Steger (*11*).

The zonal gridding approach was used to compute the recirculating viscous flow in the base region. A large grid zone was located in the base region and extended axially from the projectile base 6.35 calibers down stream. In the radial direction, the grid extended outward from the axis of symmetry to a radial location 3.5 calibers above the base corner.

To allow the flow to properly expand around the base corner, a small zone, one body diameter in length, was placed on the forebody upstream from the base corner. This grid had a one-plane overlap with the base grid and a one-to-one mapping of the grid points in the overlap region. The dimensions of the base grid were 120 axial points, 50 radial points along the base, and 50 radial points above the base corner. The forebody grid had 30 axial points and 50 radial points. Clustering of the grid points in the radial direction was performed to resolve the boundary layer on the forebody and the shear layer in the base region. The algebraic turbulence model of Chow (*13*) was applied in the base region.

5

## 3. Results

As a first step in evaluating the aerodynamic performance of a flight vehicle, the aerodynamic force and moment coefficients must be evaluated. The aerodynamic coefficients allow forces and moments due to complicated three-dimensional (3-D) motions to be characterized as a combination of aerodynamic forces and moments due to simple specific motions. The individual aerodynamic coefficients can provide insight into the aerodynamic performance of the flight vehicles.

### 3.1 Aerodynamic Moments

For symmetric missiles, the aerodynamic moments are typically modeled using the following moment expansion which is cast in a non-rolling coordinate frame (*14*). The moment formulation makes use of complex variables to separate the moment components, $\widetilde{C}_m$ and $\widetilde{C}_n$ which produce rotations in the vertical and horizontal planes, respectively. The moment about the longitudinal axis of the vehicle, $C_1$, can be treated separately.

$$\widetilde{C}_m + i\widetilde{C}_n = \left[ \left( \frac{pD}{V} \right) C_{n_{p\alpha}} - iC_{m_\alpha} \right] \widetilde{\xi} - \frac{i}{\gamma} \left[ C_{m_q} + \gamma\, C_{m_{\dot\alpha}} \right] \widetilde{\xi}' ; \tag{3}$$

$$C_1 = \left( \frac{pD}{V} \right) C_{l_p} . \tag{4}$$

In the moment formulation, the pitching moment coefficient, $C_{m_\alpha}$, produces a moment proportional to the complex angle of attack, $\widetilde{\xi}$. For small angle-of-attack flight, the cosine of the total angle of attack, $\gamma$, is nearly 1. This allows the pitch-damping moment coefficient, $C_{m_q} + C_{m_{\dot\alpha}}$, which produces moments proportional to the angular rate $\widetilde{\xi}'$, to be treated as a single coefficient. The Magnus moment coefficient, $C_{n_{p\alpha}}$, accounts for a side moment due to flow asymmetries from a combination of spin and angle of attack.

Over the past decade and a half, CFD techniques have been developed to predict the various aerodynamic coefficients previously discussed. The pitching moment coefficient, $C_{m_\alpha}$, has been routinely determined for various configurations and flight regimes for well over a decade. The prediction of the Magnus coefficients for axisymmetric projectiles at supersonic velocities was demonstrated in the early 1980s (*3*). The Magnus problem is still a research topic for complicated vehicles and at transonic velocities. More recently, techniques for predicting the pitch-damping coefficient, $C_{m_q} + C_{m_{\dot\alpha}}$, based on the solution of the Navier-Stokes equations have been developed (*5*). Although the development of a capability to predict each individual aerodynamic coefficient can be considered an important research accomplishment, it was not

6

possible to predict the stability characteristics of projectiles using CFD until a complete capability for predicting all the aerodynamic coefficients was developed. The prediction of the pitch damping coefficient represented that final step.

Figures 2–4 show results of CFD predictions for the pitching moment, Magnus moment and pitch-damping moment coefficients performed as part of the current study. Results for a free-flight Mach number of 1.8 are shown for each of the three CG locations and body lengths. In general, the CFD predictions appear to be in good agreement with the experimental data obtained from range firings of these projectiles. Results obtained at Mach 2.5 also show similar agreement with the range data.

The aerodynamic moment about the longitudinal axis of an axisymmetric vehicle can be modeled using a single aerodynamic coefficient. The roll-damping coefficient, $C_{l_p}$, represents the aerodynamic moment which opposes the spinning motion of the vehicle. For axisymmetric flight bodies, the roll-damping coefficient is produced purely by the viscous stresses acting circumferentially on the body surface. From a modeling standpoint, proper prediction of the roll-damping coefficient requires adequate grid resolution of the boundary layer. A comparison of the predicted roll-damping coefficient with range data is shown in Figure 5. Both the computational predictions and the range data show a nearly linear increase in the roll-damping coefficient with increasing body length. The predicted result shows an overprediction of ~10%. Similar results were observed at Mach 2.5. The predictions showed a <1% variation in the roll-damping coefficient at angles of attack to 6°.

## 3.2 Aerodynamic Forces

The aerodynamic forces can also be described in a manner that is analogous to the aerodynamic moments. The transverse force components $\widetilde{C}_Y$ and $\widetilde{C}_Z$ act along the $\widetilde{y}$ and $\widetilde{z}$ axes of the non-rolling coordinate frame and consist of components proportional to the complex yaw $\widetilde{\xi}$ and yawing rate $\widetilde{\xi}'$. The third force component, $C_X$, which acts along the axial direction, is loosely coupled to the transverse forces and can be treated separately. This force component consists predominantly of the drag force.

$$\widetilde{C}_Y + i\widetilde{C}_Z = -\left[ C_{N_\alpha} + i\left(\frac{p\ell}{V}\right)C_{Y_{p\alpha}} \right]\widetilde{\xi} - \frac{i}{\gamma}\left[ C_{N_q} + \gamma C_{N_{\dot{\alpha}}} \right]\widetilde{\xi}' ; \tag{5}$$

$$C_X = -C_D . \tag{6}$$

The normal force coefficient $C_{N_\alpha}$ acts normal to the longitudinal axis of the body in the pitch-plane. The force expansion also contains a damping force coefficient, $C_{N_q} + C_{N_{\dot{\alpha}}}$, that produces a force proportional to the yawing rate $\widetilde{\xi}'$. The Magnus force coefficient $C_{Y_{p\alpha}}$ accounts for the side force produced by a combination of spin and yaw.
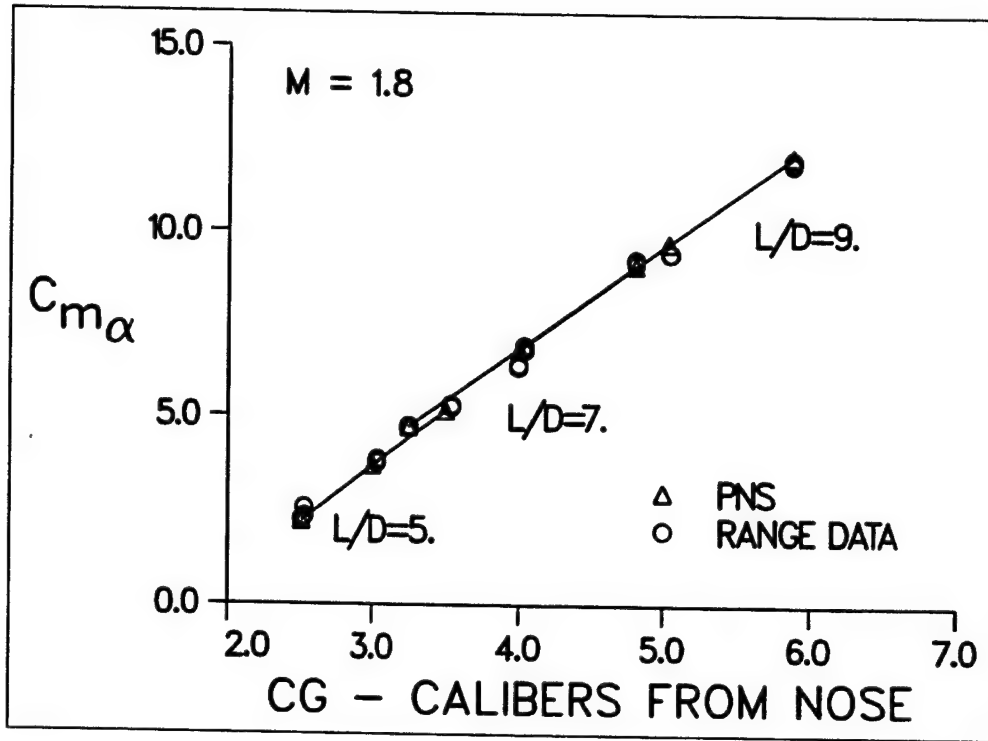
7

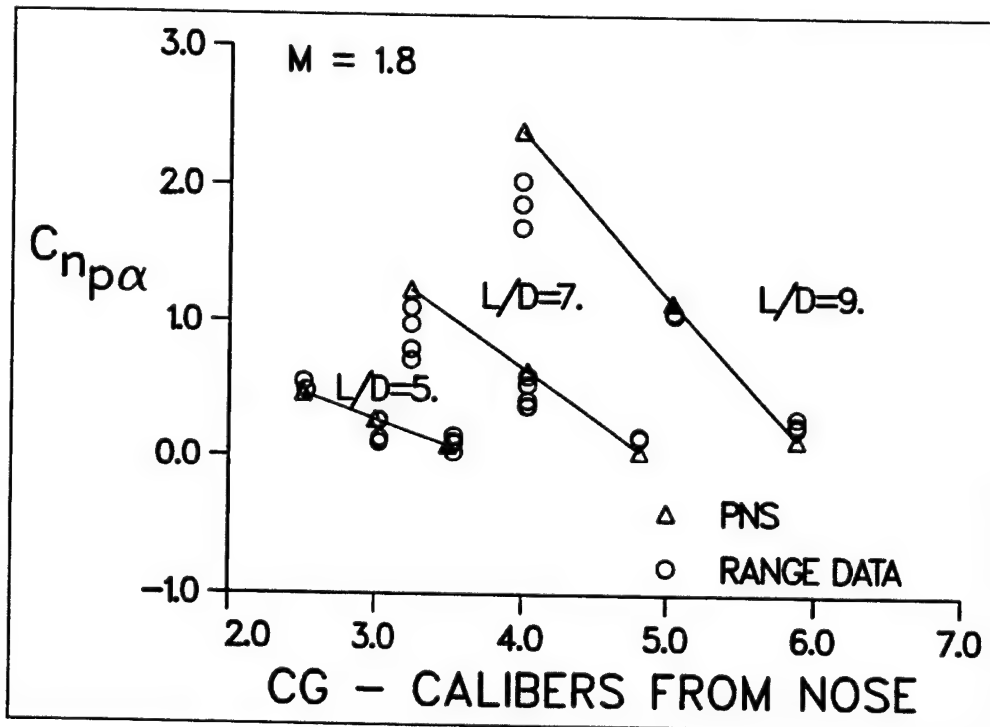Figure 2. Pitching moment coefficient vs. CG position, Mach = 1.8, ANSR.



Figure 3. Magnus moment coefficient vs. CG position, Mach = 1.8, ANSR.
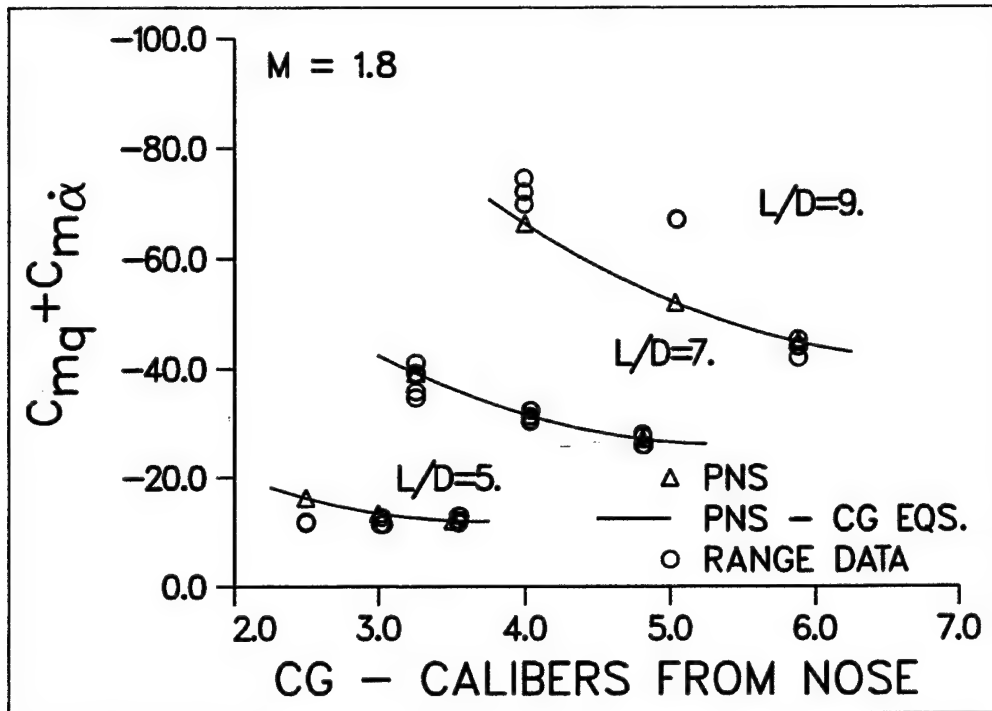
8

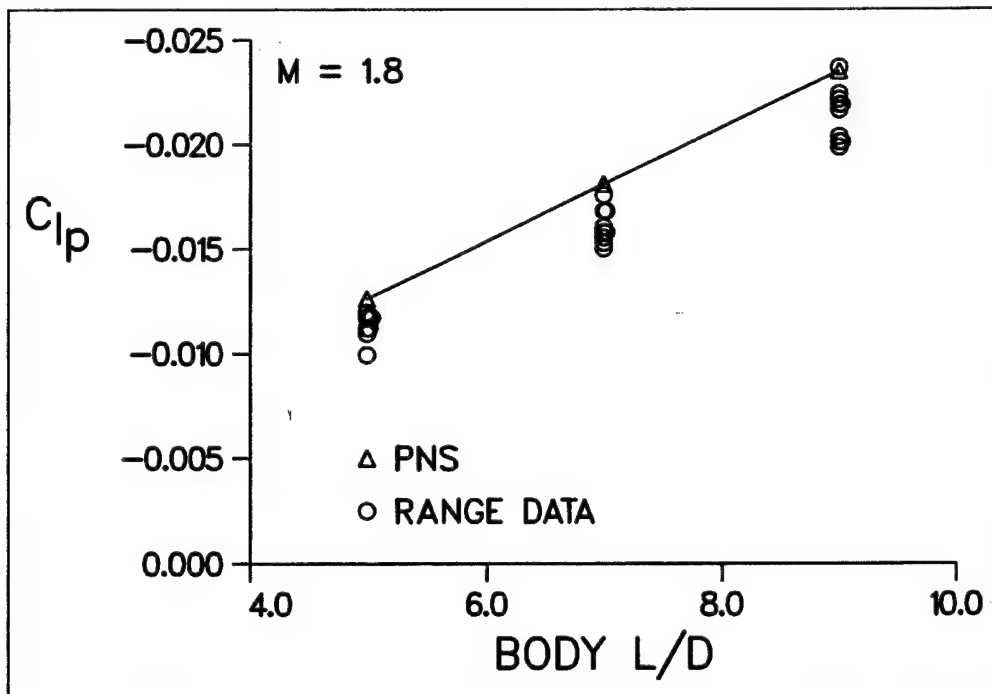Figure 4.  Pitch-damping moment coefficient vs. CG position, Mach = 1.8, ANSR.



Figure 5.  Roll-damping moment coefficient vs. body length, Mach = 1.8, ANSR.

9

Figures 6 and 7 show comparisons of the predicted and experimentally determined normal force and Magnus force coefficients at Mach 1.8 as a function of body length. The predicted normal force coefficient is predicted to within the scatter of the range data and shows little influence of body length. Both the predicted and experimentally determined Magnus force coefficient increase with body length. The Magnus force determined from the variation of the Magnus moment with CG location is ~30% less than the predictions for the L/D = 7 and L/D = 9 bodies. The Magnus force coefficients determined from the swerving (CG) motion for individual shots shows significant scatter, indicating the difficulty in accurately determining this coefficient. The pitch-damping force coefficient is not shown as it does not influence the projectile motion in a measurable manner. Comparisons of predictions with experimental data are presented by Weinacht et al. (5).
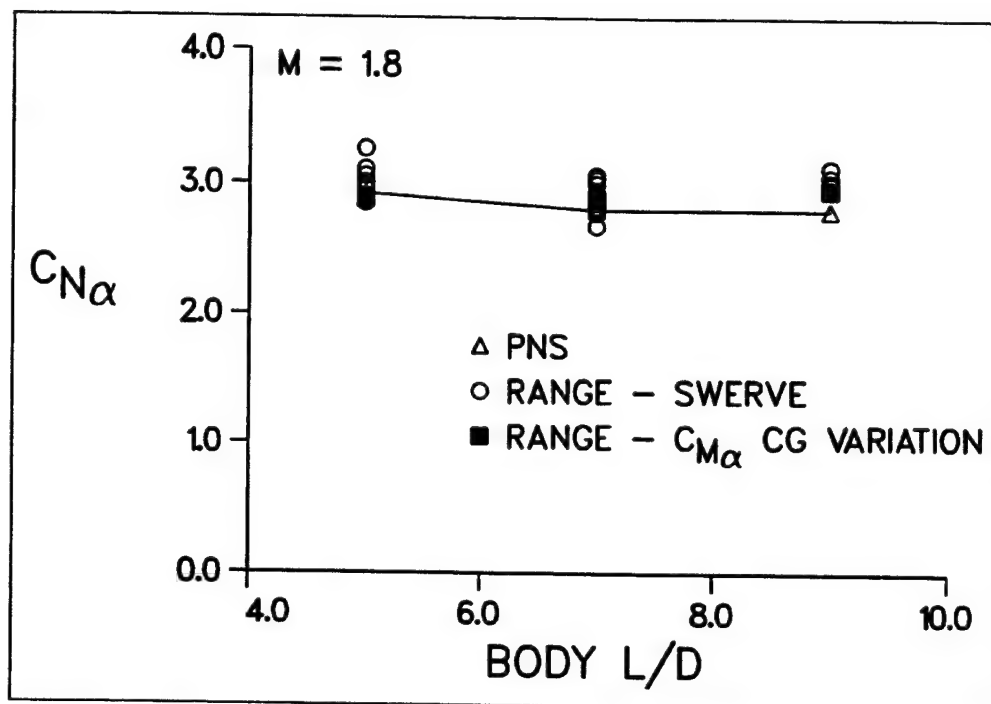


Figure 6. Normal force coefficient vs. body length, Mach = 1.8, ANSR.

The drag coefficient is also very important for predicting projectile flight performance as it is one of the primary aerodynamic coefficients affecting range. The drag coefficient is also required for the stability assessment, although its effect is small. The total drag on the projectile is composed of contributions from the forebody and the base. The forebody drag consists of both pressure and viscous drag components. The base drag results from the pressure acting on the projectile base. The forebody drag can be predicted using the PNS technique. The recirculating flow in the base region is predicted using the time-marching technique from which the base drag can be determined.
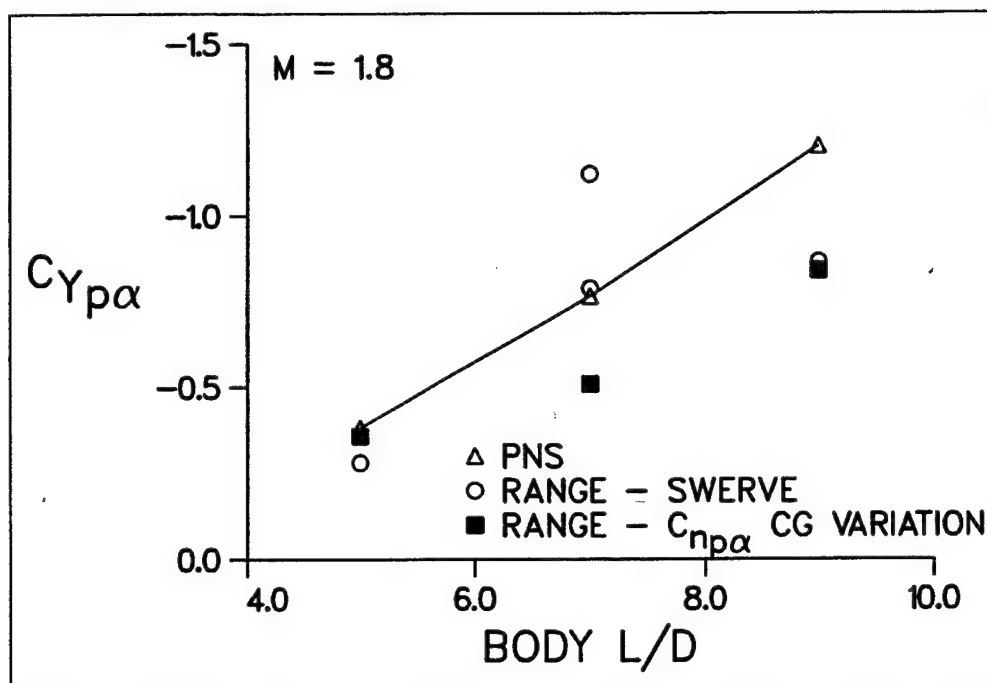
Figure 7. Magnus force coefficient vs. body length, Mach = 1.8, ANSR.

A comparison of the predicted zero-yaw drag with range results is shown in Figure 8. Drag predictions at Mach 1.8 and 2.5 are shown as a function of body length. Both the experimental results and the computational results show a slight increase in zero-yaw drag with increasing body length and decreasing Mach number. The computed drag coefficient is predicted to within the accuracy of the range data. The increase in the drag with body length is due primarily to the increase in the wetted surface of the longer body. The predicted results showed only minor variations in the base drag with body length.

At Mach 1.8 for the L/D = 9 body, the pressure and viscous forebody drag account for 39% and 25% of the total drag with the base drag accounting for the remaining 36% of the drag. Predictions of the forebody pressure drag are within 1% of previous predictions using empirical (15) or inviscid (1) approaches.

An estimate of the predicted skin friction drag, $C_{D_v}$, can be obtained using the relation developed by Charters and Kent (16).

$$C_{D_v} = -4C_{l_p}. \tag{7}$$

The estimated skin friction drag determined from the predicted roll-damping coefficient underestimates the predicted skin friction drag by 3%–10% for the predictions presented here. (This comparison gives an indication of the accuracy of the Charters and Kent relation.) The estimated skin friction obtained from the range measurements of the roll-damping coefficient is 13%–22% less than the predicted skin friction.
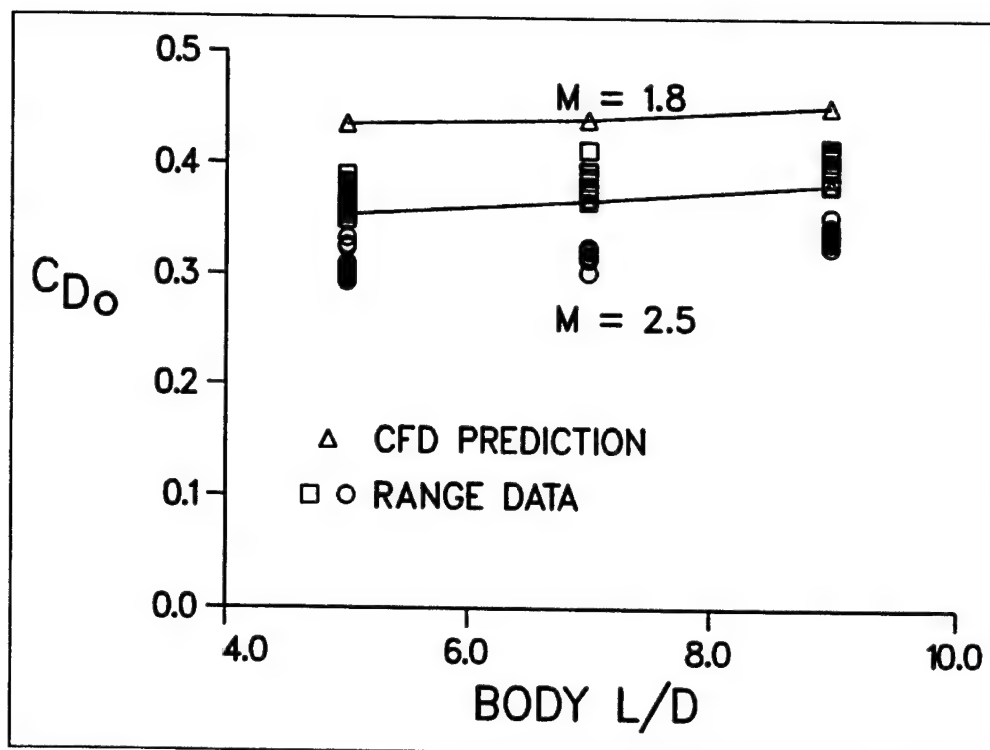
11

Figure 8. Zero-yaw drag coefficient vs. CG position, Mach = 1.8, ANSR.

Although these estimates indicate a potential 10% overprediction of the skin friction drag, the contribution to the total drag would result in an overprediction of only a few percent.

Design codes can provide a more cost-effective alternative for predicting the base drag, thus eliminating the need for a time-dependent base drag computation. The semi-empirical approach of McCoy (15) appears to overpredict the base drag by 10%–20% compared to the CFD result. When the estimated base drag is added to the forebody drag CFD predictions, the total drag is overpredicted by <9% compared to the CFD results. For stability computations, where the drag coefficient plays a minor role, acceptable accuracy can be obtained using base drag estimates.

### 3.3 Stability and Free-Flight Motion

Once the aerodynamic forces and moments have been determined, the equations of motion can be integrated and the projectile's motion can be determined for various initial conditions. Because the equations of motion are nonlinear, numerical integration is usually required to predict the projectile motion from launch to impact. These nonlinearities are typically weak, and for portions of the flight trajectory the equations can be integrated and closed-form solutions for the projectile motion can be obtained.

For a symmetric missile, the closed-form solution for the angular response as a function of the distance downrange, s, takes the following form (14):

12

$$\widetilde{\xi} = \widetilde{\xi}_g + K_1 + K_2 \approx \beta + i\alpha$$
$$K_1 = K_{10}\exp\left[i\left(\phi_{10} + \phi_1's\right) + \lambda_1 s\right] \qquad (8)$$
$$K_2 = K_{20}\exp\left[i\left(\phi_{20} + \phi_2's\right) + \lambda_2 s\right].$$

The complex variable, $\widetilde{\xi}$, consists of the vertical and horizontal components of the angle of attack, $\alpha$ and $\beta$. The angular motion contains a gravity term, $\widetilde{\xi}_g$, which is small and, for the remainder of the discussion, this term will be ignored. The second and third terms of equation 8 are expressions of the amplitudes of two components of the angular motion, referred to as the fast and slow modes, respectively. The complex angle of attack, $\widetilde{\xi}$, can be displayed graphically along with the fast and slow mode arms, $K_1$ and $K_2$. Graphically, the solution is shown by Figure 9 and is referred to as a damped epicycle. It is helpful to regard this figure as the path that the nose of the projectile would follow as it flies downrange. The fast and slow mode frequencies of the motion, $\phi_1'$ and $\phi_2'$, and the damping rates, $\lambda_1$ and $\lambda_2$, are functions of the aerodynamic coefficients, projectile spin rate, and inertial properties of the body. Generally speaking, the frequencies are influenced by the pitching moment coefficient, while the damping is influenced by the Magnus and pitch damping coefficients. The equation also contains the initial amplitudes, $K_{10}$ and $K_{20}$, and phase angles, $\phi_{10}$ and $\phi_{20}$, which result from applying the initial conditions during the integration of the equations.
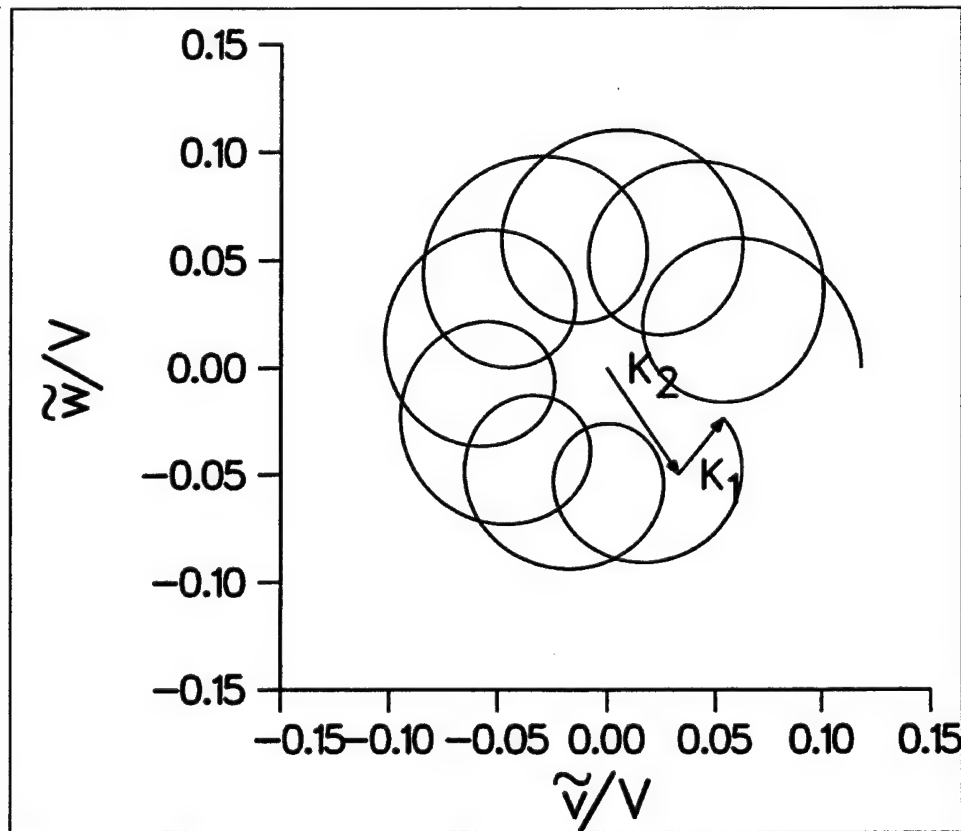


Figure 9. Projectile angular motion epicycle.

13

Using the predicted aerodynamic coefficients, the fast and slow mode damping and frequencies were computed for the various body lengths, CG positions, launch Mach numbers, and spin rates. Figure 10 shows the predicted slow mode frequency plotted against the experimentally determined value. (The results are plotted in this fashion due to the large number of parameters considered here.) Points that fall close to the solid line indicate that the predicted value is close to the experimentally determined value. There is good agreement between prediction and experiment. The slow mode frequency represents the critical comparison for the frequencies because the fast mode frequency is dominated by the spin rate, which is essentially an input parameter.
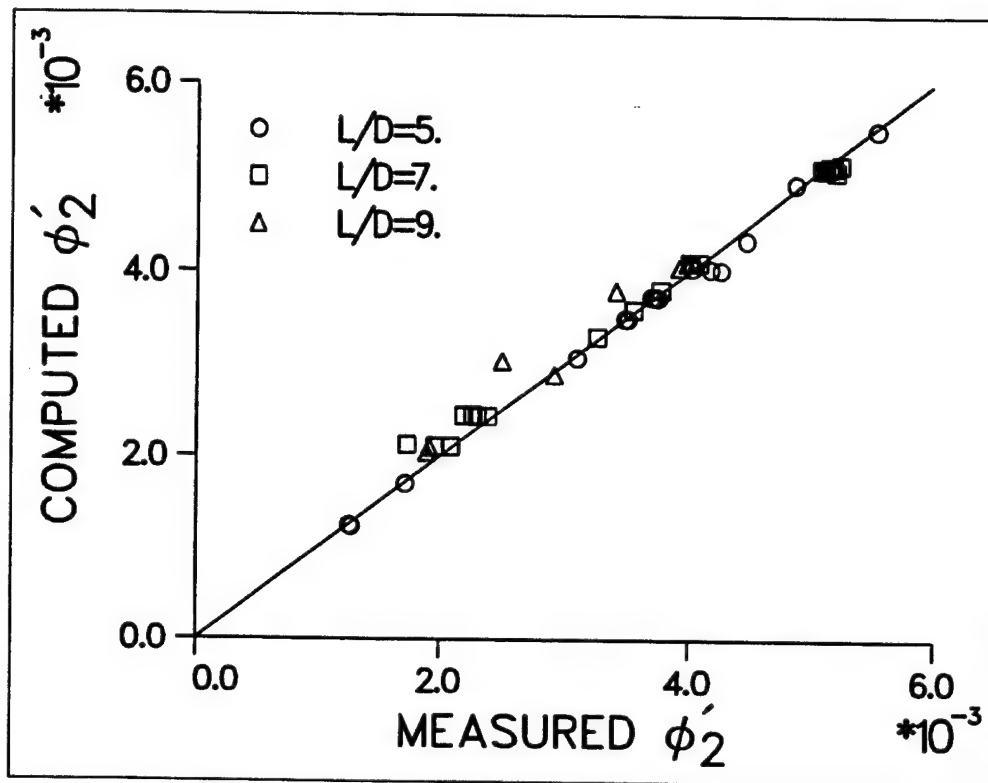


Figure 10. Comparison of computed slow mode frequency with measured slow mode frequency, ANSR.

Figures 11 and 12 show comparisons of the predicted slow and fast mode damping of each of the bodies. The data are scattered about the solid line, indicating that the prediction is generally in good agreement with the experiment. No consistent bias between the computation and experimental data is seen. This indicates that there is no consistent underprediction or overprediction of the damping rates. Much of the scatter in the data is attributed to the uncertainty in the experimental data rather than inaccuracies in the computational approach.

Generally, from a design standpoint, predicting and controlling damping rates, rather than the frequencies, is a primary consideration. One desirable requirement is that the damping rates, $\lambda_1$ and $\lambda_2$, be negative so that the angular motion does not grow during the projectile's flight.
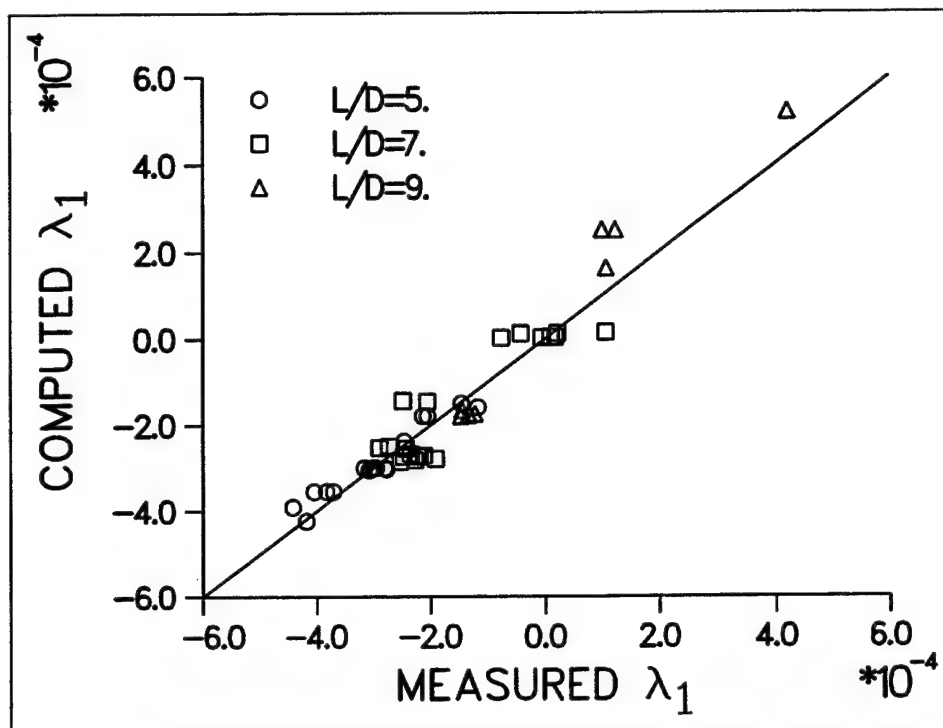
14

Figure 11. Comparison of computed fast mode damping with measured fast mode damping, ANSR.
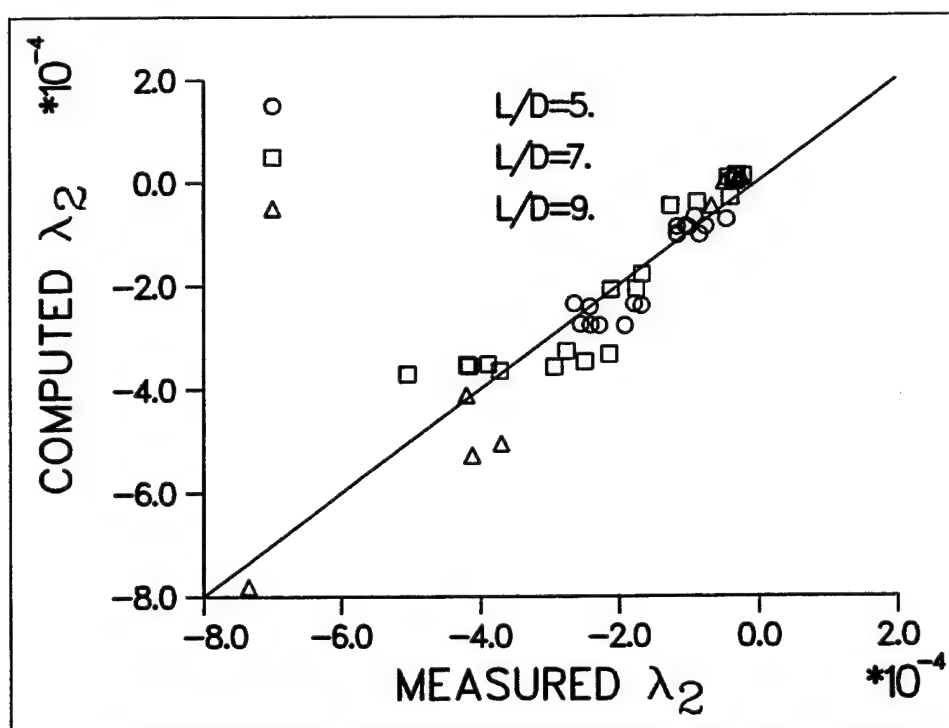


Figure 12. Comparison of computed slow mode damping with measured slow mode damping, ANSR.

15

By algebraically manipulating the equations for the damping rates, three necessary conditions can be derived, which will ensure that the damping rates are negative. Two of these conditions are shown in equation 9:

$$s_g > 1; \quad s_g = f(p, C_{m_\alpha})$$
$$s_g < s_d(2 - s_d); \quad s_d = f(C_{n_{p\alpha}}, C_{m_q} + C_{m_{\dot{\alpha}}}). \tag{9}$$

The first condition states that the gyroscopic stability factor, $s_g$, must be >1 for the projectile to be gyroscopically stable. The second condition also places an additional constraint on the gyroscopic stability factor through the dynamic stability factor, $s_d$. As shown in these equations, the gyroscopic stability and dynamic stability factors are functions of the aerodynamic coefficients. Additionally, the gyroscopic stability factor is also a function of the projectile spin rate, p. For typical spin-stabilized projectiles that are statically unstable, the two stability criteria can be satisfied by adjusting the spin rate of the projectile, as long as the dynamic stability factor is between 0 and 2. If the dynamic stability factor is outside this bound, the projectile cannot be stabilized using spin. A third condition for stability essentially requires that the pitch damping coefficient, $C_{m_q} + C_{m_{\dot{\alpha}}}$ to be negative. This condition is rarely violated in practice.

The constraints on the gyroscopic stability and dynamic stability factors discussed previously can be shown graphically on what is often termed a "stability plot." Figures 13 and 14 show plots of the results as measured in the aerodynamics range and obtained from the computation. Shown on the plot are results for the each of the three CG locations for the three different length bodies, various spin rates, and for Mach numbers of 1.8 and 2.5. For each firing, experimental and computational values of the gyroscopic stability factor, $s_g$, and the dynamic stability factor, $s_d$, were computed. It is important to realize that for a given set of conditions (body length, spin rate, launch Mach number), the computational results will yield a unique value. However, because of the scatter associated with the experimental data, each firing yields a slightly different value. Thus, the experimental results give the appearance of having more data. It is important to realize this when comparing the two sets of plots.

The computational and experimental results presented in these figures show that this family of projectiles is statically unstable ($s_g > 0$), but has been made gyroscopically stable by appropriate selection of the spin rate ($s_g > 1$). The results also show that all of the L/D = 5 projectiles are dynamically stable. (The region of dynamic stability is denoted by the shaded area on these plots.) The results indicate that several of the L/D = 7 and L/D = 9 projectiles are marginally stable, though these can be stabilized by selection of a higher spin rate because the dynamic stability factor is between 0 and 2. Several of the L/D = 9 bodies are dynamically unstable and cannot be stabilized by changing the spin rate. Further examination of the data revealed that
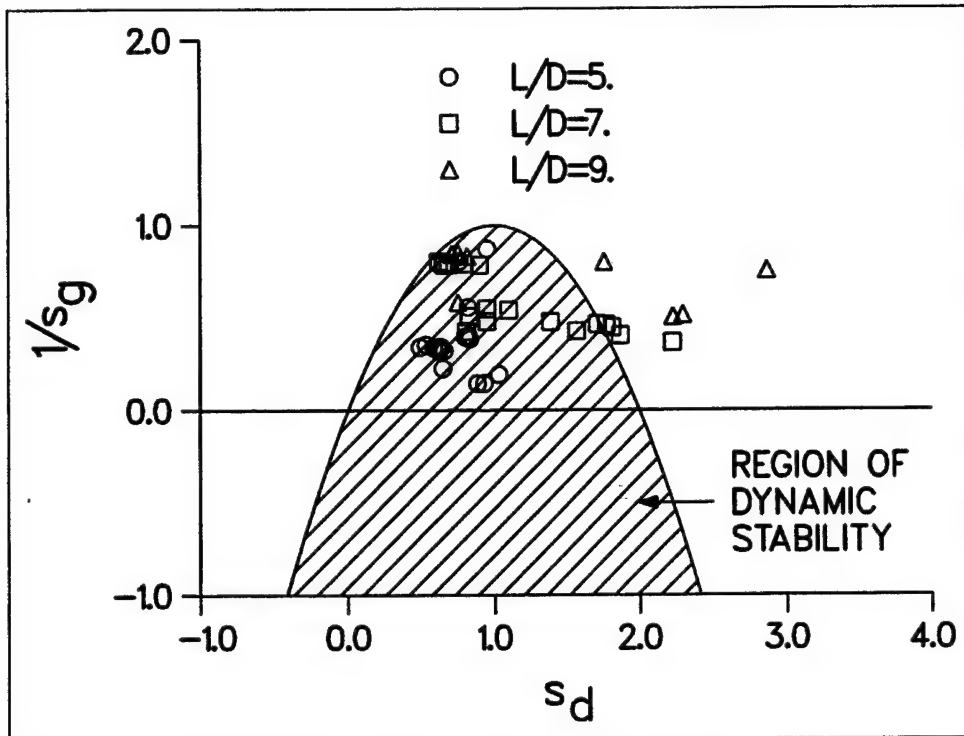
16

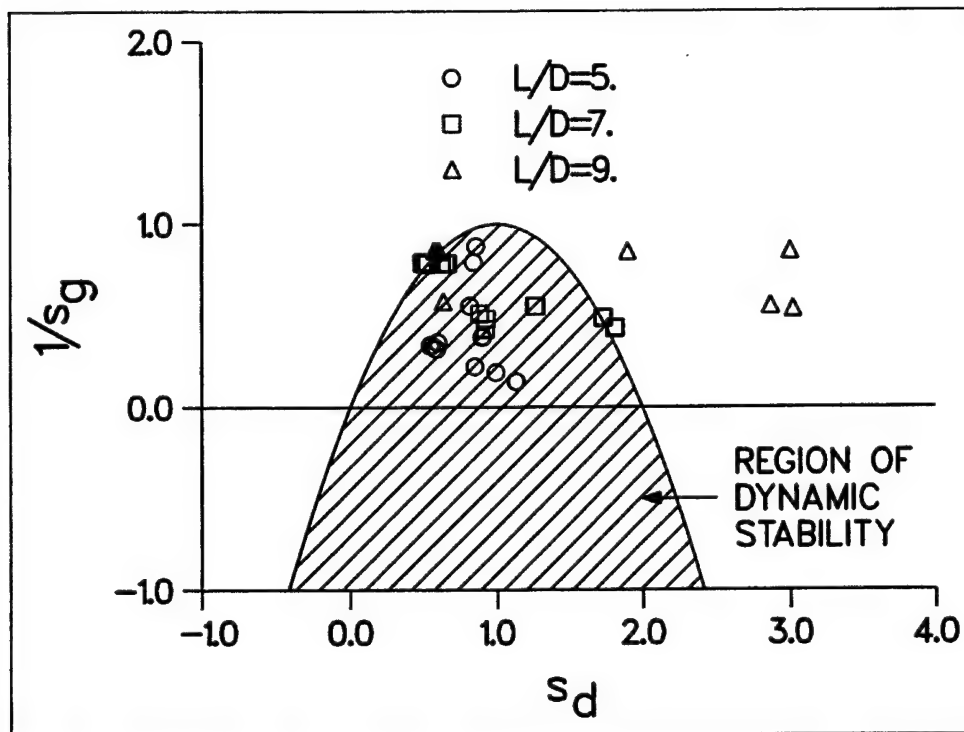Figure 13. Stability plot for ANSR from range data.



Figure 14. Stability plot for ANSR from CFD predictions.

17

the L/D = 9 bodies which could not be stabilized all had the CG located in the aftmost position. It is important to note that the computational approach correctly predicts the stability characteristics of the various configurations for the conditions of dynamic stability, marginal dynamic stability, and dynamic instability. This demonstrates the utility of the computational approach for the purposes of stability prediction.

With the prediction of the frequencies and damping rates of the angular motion, the angular motion itself can be predicted and compared with the motion measured in the aerodynamics range. Figures 15 and 16 show the angular motion of a 5-caliber-long projectile launched at Mach 1.8 and a 7-caliber projectile launched at Mach 2.5. These 3-D plots display the vertical and horizontal components of angle of attack, $\alpha$ and $\beta$, as a function of the distance downrange, Z. The thickened curve displays the 3-D motion. Two-dimensional projections of the motion in the vertical and horizontal planes are also shown. It is useful to regard the curves shown here as the path traversed by the nose of the projectile as it flies downrange. The motion predicted using the CFD-derived aerodynamic coefficients is denoted by the solid lines, while the motion obtained from the range firings is shown by the circular symbols. The agreement between the two motions is excellent. Comparisons of the in-flight motion at other flight conditions and for the other body geometries also showed good agreement with the experimental data.
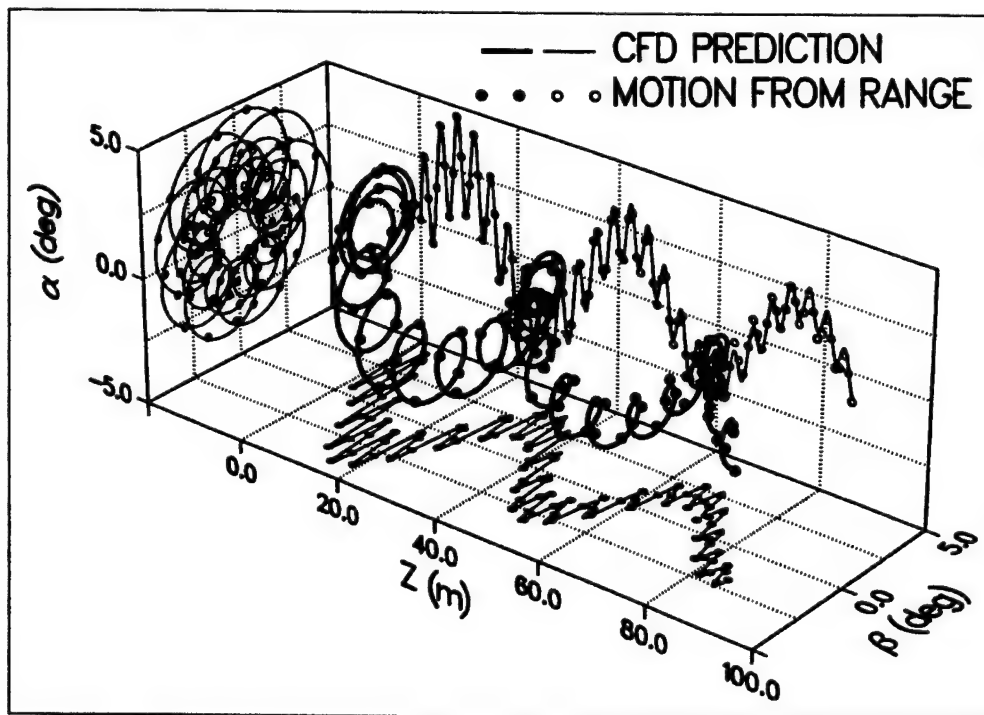


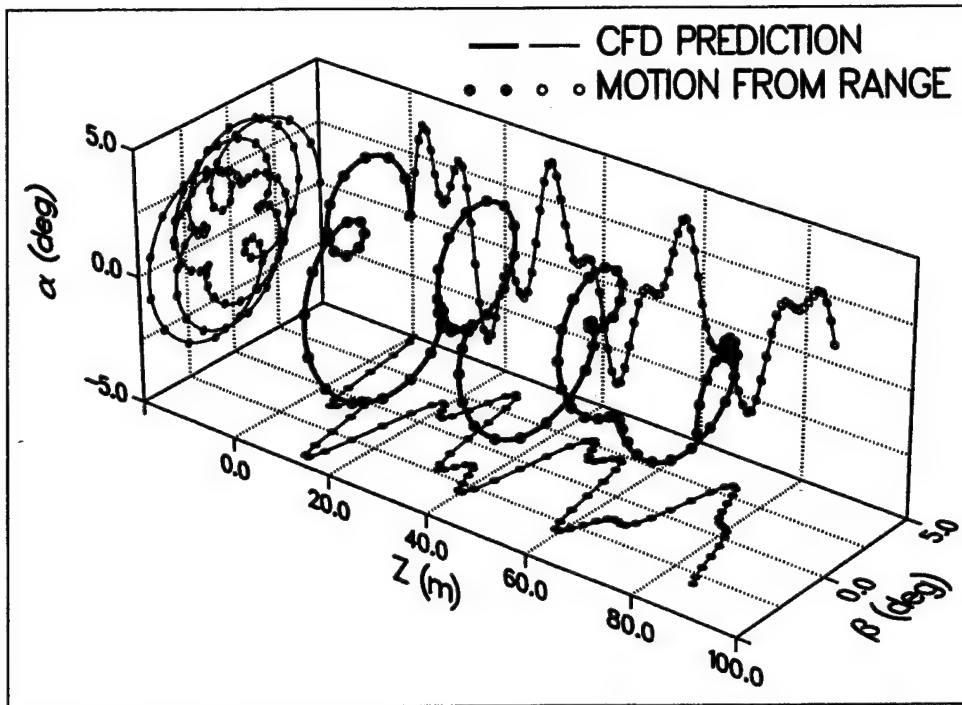Figure 15. In-flight angular motion, 5-caliber body, Mach 1.8.

18

Figure 16. In-flight angular motion, 7-caliber body, Mach 2.5.

## 4. Conclusion

CFD provides an alternate means for determining the aerodynamic performance of projectiles. This will allow projectiles to be designed with a reduced requirement for manufacturing models and performing test firings. As a test case, the aerodynamic performance of a family of axisymmetric projectiles in supersonic flight was examined. The predictions showed good agreement with range data for individual aerodynamic coefficients. Using these coefficients, the frequencies and damping rates of the angular motion were computed. The results showed good correlation with the experimental data for various body lengths, center of gravity locations, Mach numbers and spin rates. The aerodynamic coefficients were also used to predict gyroscopic and dynamic stability factors. The computational approach correctly distinguished the conditions of dynamic instability, marginal dynamic stability, and dynamic stability. As a final comparison, the in-flight angular motion for individual firings was compared with range data and showed good agreement. The results are believed to properly represent the capability for predicting the linear aerodynamics for the high-speed low angle-of-attack flight of aerodynamically smooth axisymmetric projectiles. Additional computational effort (and, in some cases, additional research) may be required to establish the same capability at subsonic and transonic velocities or for complex geometries.

19

# 5. References

1. Murphy, C. H.; Schmidt, L. E. *The Effect of Length on the Aerodynamic Characteristics of Bodies of Revolution in Supersonic Flight*; Report No. 876; U.S. Army Ballistic Research Laboratories: Aberdeen Proving Ground, MD, August 1953.

2. Nietubicz, C. J.; Opalka, K. *Supersonic Wind Tunnel Measurements of Static and Magnus Aerodynamic Coefficients for Projectile Shapes With Tangent and Secant Ogive Noses*; ARBRL-MR-02991; U.S. Army Ballistic Research Laboratory: Aberdeen Proving Ground, MD, February 1980.

3. Sturek, W. B.; Schiff, L. B. Computations of the Magnus Effect for Slender Bodies in Supersonic Flight. American Institute of Aeronautics and Astronautics, Reston, VA, August 1980; AIAA Paper 80-1586-CP.

4. Sturek, W. B.; Mylin, D. C. Computational Parametric Study of the Magnus Effect on Boattailed Shell at Supersonic Speeds. American Institute of Aeronautics and Astronautics, Reston, VA, August 1981; AIAA Paper 81-1900.

5. Weinacht, P.; Sturek, W. B.; Schiff, L. B. Navier-Stokes Predictions of Pitch Damping for Axisymmetric Projectiles. *Journal of Spacecraft and Rockets* **1997**, *34* (6), 753–761.

6. Schiff, L. B.; Steger, J. L. Numerical Simulation of Steady Supersonic Viscous Flow. *AIAA Journal* **1980**, *18* (12), 1421–1430.

7. Beam, R.; Warming, R. F. An Implicit Factored Scheme for the Compressible Navier-Stokes Equations. *AIAA Journal* **1978**, *16* (4), 85–129.

8. Baldwin, B. S.; Lomax, H. Thin Layer Approximation and Algebraic Model for Separated Turbulent Flows. American Institute of Aeronautics and Astronautics, Reston, VA, January 1978; AIAA Paper 78-257.

9. Rai, M. M.; Chaussee, D. S. New Implicit Boundary Procedure: Theory and Applications. American Institute of Aeronautics and Astronautics, Reston, VA, January 1983; AIAA Paper 83-0123.

10. Ying, S. X.; Steger, J. L.; Schiff, L. B.; Baganoff, D. Numerical Simulation of Unsteady, Viscous, High-Angle-of-Attack Flows Using a Partially Flux-Split Algorithm. American Institute of Aeronautics and Astronautics, Reston, VA, August 1986; AIAA Paper 86-2179.

11. Sahu, J.; Steger, J. L. Numerical Simulation of Three-Dimensional Transonic Flows. *International Journal for Numerical Methods in Fluids* **1990**, *10*, 855–873.

12. Steger, J. L.; Warming, R. F. Flux Vector Splitting of the Inviscid Gasdynamic Equations With Application to Finite-Difference Methods. *Journal of Computational Physics* **1981**, *40*, 263–293.

13. Chow, W. L. *Improvement on Numerical Computation of the Thin-Layer Navier-Stokes Equation With Special Emphasis on the Turbulent Base Pressure of a Projectile in Transonic Flight Condition*; Contract Report No. DAAG29-81-D-0100; University of Illinois, Urbana-Champaign: Urbana, IL, November 1985.

14. Murphy, C. H. *Free Flight Motion of Symmetric Missiles*; Report No. 1216; U.S. Army Ballistic Research Laboratories: Aberdeen Proving Ground, MD, July 1963.

15. McCoy, R. L. *MC DRAG—A Computer Program for Estimating the Drag Coefficients of Projectiles*; ARBRL-TR-02293; U.S. Army Ballistic Research Laboratory: Aberdeen Proving Ground, MD, February 1981.

16. Charters, A. C.; Kent, R. H. *The Relation Between the Skin Friction and the Spin Reducing Torque*; Report 287; U.S. Army Ballistic Research Laboratories: Aberdeen Proving Ground, MD, July 1942.

# List of Abbreviations and Symbols

$a_\infty$        Freestream speed of sound

$C_D$        Drag coefficient

$C_{D_0}$        Zero-yaw drag coefficient

$C_{D_v}$        Viscous drag coefficient

$C_l$        Net roll moment coefficient

$C_{l_p}$        Roll-damping moment coefficient, $\dfrac{\partial C_l}{\partial\left(\dfrac{pD}{V}\right)}$

$C_m$        Pitching moment coefficient, $\dfrac{\overline{M}}{\dfrac{1}{2}\rho V^2 S_{ref} D}$

$C_{m_\alpha}$        Pitching moment coefficient slope with respect to angle of attack, $\dfrac{\partial C_m}{\partial\alpha}$

$C_{m_{\dot\alpha}}$        Pitch-damping moment coefficient slope, $\dfrac{\partial C_m}{\partial\left(\dfrac{\dot\alpha D}{V}\right)}$

$C_{m_q}$        Pitch-damping moment coefficient slope, $\dfrac{\partial C_m}{\partial\left(\dfrac{qD}{V}\right)}$

$C_{m_q}+C_{m_{\dot\alpha}}$        Pitch-damping moment coefficient

$C_n$        Side moment coefficient

$C_{n_{p\alpha}}$        Magnus moment coefficient, $\dfrac{\partial^2 C_n}{\partial\left(\dfrac{pD}{V}\right)\partial\alpha}$

$C_N$        Normal force coefficient, $\dfrac{\overline{F}}{\dfrac{1}{2}\rho V^2 S_{ref}}$

22

$C_{N_\alpha}$ — Normal force coefficient slope with respect to angle of attack, $\dfrac{\partial C_N}{\partial \alpha}$

$C_{N_{\dot\alpha}}$ — Pitch-damping force coefficient slope, $\dfrac{\partial C_N}{\partial\left(\dfrac{\dot\alpha D}{V}\right)}$

$C_{N_q}$ — Pitch-damping force slope, $\dfrac{\partial C_N}{\partial\left(\dfrac{q D}{V}\right)}$

$C_{N_q} + C_{N_{\dot\alpha}}$ — Pitch-damping force coefficient

$C_X$ — Axial force coefficient

$C_Y, C_Z$ — Transverse force coefficient in $y$ and $z$ direction

$C_{Y_{p\alpha}}$ — Magnus force coefficient

$D$ — Reference diameter

$e$ — Total energy per unit volume

$\hat{E}, \hat{F}, \hat{G}$ — Flux vectors in transformed coordinates

$\overline{F}$ — Force

$\hat{H}$ — Source term in Navier-Stokes equations due to rotating coordinate frame

$K_1, K_2$ — Amplitude of fast and slow yaw arms

$K_{10}, K_{20}$ — Initial amplitude of fast and slow yaw arms

$L$ — Body length

$\overline{M}$ — Moment

$M$ — Freestream Mach number

$p$ — Spin rate, as used in roll equations

$q$ — Transverse angular rate of body, as used in flight mechanics equations

$q$ — Vector of dependent variables, as used in Navier-Stokes equations

$Re$ — Reynolds number, $a_\infty \rho_\infty D / \mu_\infty$

$s$ — Distance downrange normalized by reference length

| | |
|---|---|
| $s_d$ | Dynamic stability factor |
| $s_g$ | Gyroscopic stability factor |
| $S_{ref}$ | Reference area, $S_{ref} = \dfrac{\pi D^2}{4}$ |
| $\hat{S}$ | Viscous flux vector |
| t | Time |
| u, v, w | Velocity components in the x, y, z directions |
| V | Freestream velocity |
| x, y, z | Axial, horizontal, and vertical coordinates |
| $y^+$ | Nondimensional boundary layer coordinate |
| Z | Dimension downrange distance |

## Greek Symbols

| | |
|---|---|
| $\alpha$ | Angle of attack |
| $\dot{\alpha}$ | Angular rate associated with angle of attack |
| $\beta$ | Yaw angle |
| $\gamma$ | Cosine of total angle of attack |
| $\lambda_1, \lambda_2$ | Fast and slow mode damping rates |
| $\mu,$ | Viscosity |
| $\xi, \eta, \zeta$ | Transformed coordinates in the Navier-Stokes equations |
| $\tilde{\xi}$ | Complex angle of attack |
| $\tilde{\xi}_g$ | Complex angle-of-attack component induced by gravity |
| $\rho$ | Density |
| $\phi_{10}, \phi_{20}$ | Phase angle of fast and slow mode arms |
| $\phi_1', \phi_2'$ | Fast and slow mode frequencies |

## Superscripts

$(\dot{\ })$           Rate of change with respect to time

$(\ )'$           Rate of change with respect to space

$(\tilde{\ })$           Referenced to non-rolling coordinate frame


## Subscripts

$\infty$           Quantity evaluated at freestream conditions

INTENTIONALLY LEFT BLANK.